Comput Mech (2011) 47:573–590
DOI 10.1007/s00466-010-0563-4

ORIGINAL PAPER

Forming forces in single point incremental forming: prediction by finite element simulations, validation and sensitivity

C. Henrard · C. Bouffioux · P. Eyckens · H. Sol · J. R. Duflou · P. Van Houtte · A. Van Bael · L. Duchêne · A. M. Habraken

Received: 18 December 2009 / Accepted: 26 November 2010 / Published online: 31 December 2010

Abstract The aim of this article is to study the accuracy of finite element simulations in predicting the tool force occurring during the single point incremental forming (SPIF) process. The forming of two cones in soft aluminum was studied with two finite element (FE) codes and several constitutive laws (an elastic–plastic law coupled with various hardening models). The parameters of these laws were identified using several combinations of a tensile test, shear tests, and an inverse modeling approach taking into account a test similar to the incremental forming process. Comparisons between measured and predicted force values are performed. This article shows that three factors have an influence on force prediction: the type of finite element, the constitutive law and the identification procedure for the material parameters. In addition, it confirms that a detailed description of the behavior occurring across the thickness of the metal sheet is crucial for an accurate force prediction by FE simulations, even though a simple analytical formula could provide an otherwise acceptable answer.

Keywords Single point incremental forming · Finite element modeling · Force prediction · Material parameters identification · Inverse modeling

C. Henrard (✉) · C. Bouffioux · L. Duchêne · A. M. Habraken
ArGEnCo, Université de Liège, Chemin des Chevreuils 1, 4000 Liège, Belgium
e-mail: Christophe.Henrard@samtech.com

A. M. Habraken
e-mail: Anne.Habraken@ulg.ac.be

Present Address:
C. Henrard
Samtech S.A., Rue des Chasseurs Ardennais 8, 4031 Liège, Belgium

P. Eyckens · P. Van Houtte · A. Van Bael
MTM, Katholieke Universiteit Leuven, Kasteelpark Arenberg 44, Bus 02450, 3001 Heverlee, Belgium

H. Sol
MEMC, Vrije Universiteit Brussel, Pleinlaan 2, 1050 Brussels, Belgium

J. R. Duflou
PMA, Katholieke Universiteit Leuven, Celestijnenlaan 300 B, 3001 Heverlee, Belgium

A. Van Bael
KHLim (Limburg Catholic University College), Campus Diepenbeek, Agoralaan gebouw B, 3590 Diepenbeek, Belgium

1 Introduction

Unlike many other sheet metal forming processes, incremental forming does not require any dedicated dies or punches to form a complex shape and is therefore well adapted to rapid prototyping, as confirmed by several authors [1–5]. The process uses a standard smooth-end tool, the diameter of which is far smaller than the part being made, and which is mounted on a three-axis CNC milling machine, a multi-axis robot, or a dedicated machine.

The sheet metal blank is clamped around its edges using a blank-holder. During the forming process, the tool moves along a succession of contours, which follow the final geometry of the part, and deforms the sheet incrementally into its desired shape. A schematic description of the process is shown in Fig. 1a and b and an example of the tool path in Fig. 2.

The prediction of forming forces occurring during incremental forming is a crucial piece of information, since it governs the choice of the hardware setup. Indeed, most classic milling machines only tolerate a relatively limited axial force and exceeding this limit could potentially damage the

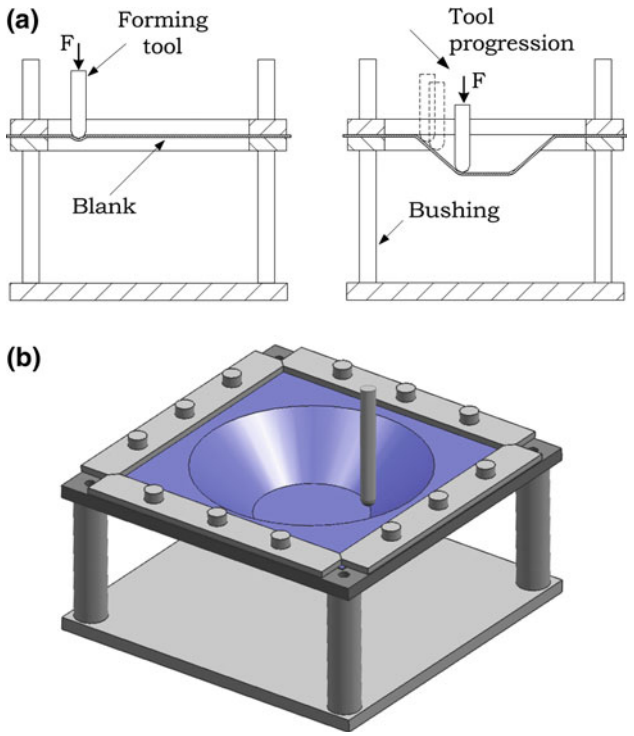

Fig. 1 Single point incremental forming (**a**) schematic description of the process [6], (**b**) sheet metal clamping device (picture courtesy of Johan VERBERT, KUL)

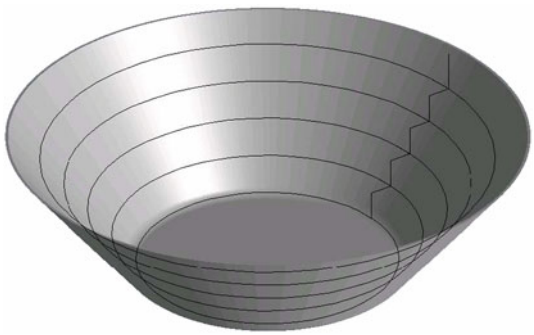

Fig. 2 Tool path for a conical shape [7]

machine or, at least, its bearings. Furthermore, performing the SPIF process on an industrial robot with more than three axes causes additional part inaccuracies due to the limited stiffness of the hardware set-up, unless the force acting on the forming tool can be predicted and compensated for [8].

Several papers have been published about prediction and analysis of forming forces as a function of experimental setup parameters [9–12]. Duflou et al. [13] presented a model for force prediction during the forming of a cone as a function of the step-down amplitude, the wall angle, the tool diameter and the sheet thickness. This model was based on a simple regression equation that could predict the peak, steady-state, and in-plane forces with a high degree of confidence. For more complex geometries, they could not reach such a simple equation but showed that the geometry of the part should be taken into account in the model. This work was later continued by Aerens et al. [8]. They were able to develop a new model with a highly efficient strategy to identify the parameters based on experimental measurements. Several materials were tested. For each material, the authors fitted an analytical formula able to predict the level of the steady-state tool force accurately for various part geometries. The ultimate tensile strength of a given material seemed to be the key material parameter governing the level of the forces. As verified below, the application of these simple analytical formulas is quite efficient as well for the two cones studied in this article.

In Flores et al. [14], the effect of the constitutive law on the force prediction by FE simulations of SPIF was studied. A strong discrepancy between the simulation results based on an elastic–plastic law with isotropic or kinematic hardening model could be seen, demonstrating the high sensitivity of the force prediction. In the present paper, experimental results will be compared to the forces predicted using both shell and brick elements linked to different yield loci coupled with various hardening models. A section will also be devoted to the material parameter identification method which can affect the FE predictions.

Two different cones have been analyzed, whose wall angles α (Fig. 3) of 20° and 60° were chosen because of the following observations by Eyckens et al. [15]. The authors experimentally quantified the through-thickness shear occurring during SPIF by drilling small holes into the sheet prior to forming and by measuring their orientation at the end of the forming process. They demonstrated that the through-thickness shear characterized by the angle γ_{13} is negative (see Fig. 3) and that it becomes closer to 0 with a decreasing wall angle α (Fig. 4a), which means that this through-thickness shear component would be nearly negligible for a cone with a wall angle of 20° and large for a cone with a wall angle of 60°. On the other hand, the through-thickness shear angle γ_{23} in the perpendicular plane, i.e., the plane containing the local direction of the tool movement, showed to be practically independent on the wall angle in the tested range (Fig. 4b).

In their paper Emmens and van den Boogaard [16] focus on the implications of the through-thickness shear on the strain definition. The presence of through-thickness shear will cause the principal strains to be no longer contained within the sheet surface and the local normal direction for the sheet. Also, the von Mises equivalent strain, which is used in many hardening law definitions, can no longer be obtained from the surface strains alone.

Allwood et al. [17] developed a simplified version of incremental forming called paddle forming. By modeling this process with a finite element (FE) method, the authors were able to demonstrate that the through-thickness shear is significant in the direction of the tool movement. These

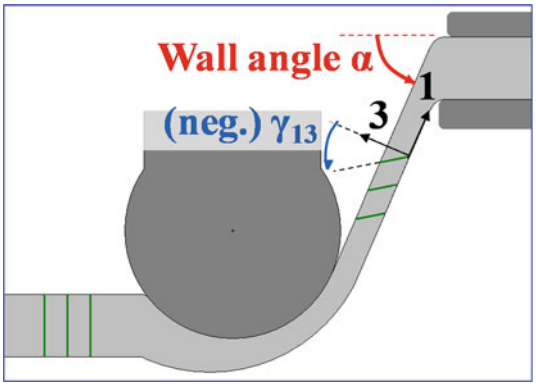

Fig. 3 Definition of wall angle α and a negative through-thickness shear angle γ_{13}; material lines initially aligned across the sheet thickness direction are illustrated in both the cone's wall and its flat part

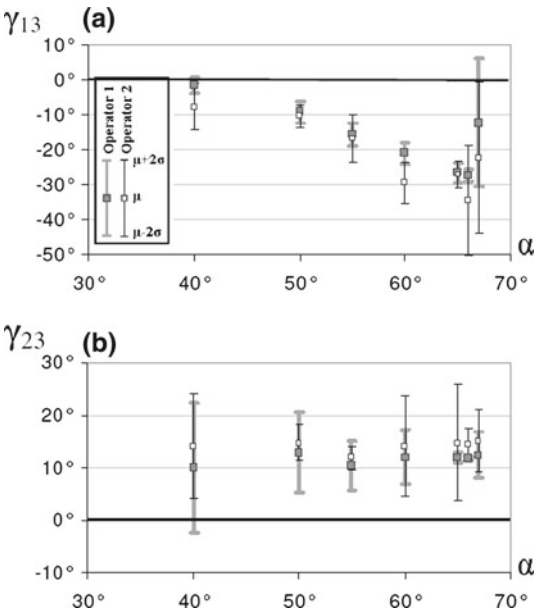

Fig. 4 Measurement of the through-thickness shear angles (**a**) γ_{13} and (**b**) γ_{23} as a function of wall angle α [15]

authors attributed this phenomenon to the fact that the material on the top surface of the sheet metal tends to move in the direction of the tool displacement. In a different article [18], the same authors incorporated through-thickness shear into a Marciniak–Kuczynski (MK) model. They proved that the forming limit curve increases with increasing through-thickness shear γ_{13} or γ_{23}, regardless of the direction, positive or negative, of the latter.

Similarly, Eyckens et al. [15,19,20] also extended the MK framework to include through-thickness shear, even though the authors used very different assumptions. According to this model, the shear component in plane 23 (see Fig. 3) has a much higher effect on the forming limit diagram (FLD) than the one in plane 13. Formability predictions of both these models are thus fundamentally different. For the moment, there is a lack of experimental evidence that proves or disproves the dependence of the formability on the direction of through-thickness shear.

Besides through-thickness shear, other mechanisms have been proposed to explain the high formability in SPIF, an overview of which is given in Emmens and van den Boogaard [21].

After this introduction, which explained the interest of force prediction in SPIF as well as of the non negligible effect of the through-thickness shear during the process, Sect. 2 will present the experiments. Different simulation parameters (element type, boundary conditions and meshes) are presented in Sect. 3 as well as the constitutive laws used. Then Sect. 4 will describe how the parameters of the material behavior model have been identified. The simulation predictions of cones 20° and 60° are summarized in Sect. 5 and compared to experimental results. A discussion of these results will provide guidelines to accurate force predictions with FEM.

2 Experiments

2.1 Experimental set-up

Figure 5 shows the standard three-axis CNC ACIERA milling machine with a horizontal spindle used to form the cones. For incremental forming, the tool speed was reduced to 2,000 mm/min and the spindle rotation speed was set so that a rolling contact was established at half the theoretical contact height along the cone wall. That meant, according to formula (1) in [22], using a rotation speed between 80 and 250 rpm depending on the wall angle of the part being made and on the tool size.

The tool was a hemispherical head mounted on a shaft and was manufactured by Uddeholm [23] using a chromium molybdenum tungsten and vanadium alloyed high-speed steel, called Vanadis 23.

The forces acting on the tool were measured using a force platform [8,24]. This platform was a Kistler 9265B six-component force dynamometer, used with a multichannel charge amplifier 5017A capable of measuring a vertical force between −15 and 30 kN and two horizontal forces of ±15 kN (see Fig. 6). The stiff dynamometer makes it possible to measure the three orthogonal components of the forming force F_x, F_y and F_z (see Fig. 6). The axial force F_z (applied in the axial direction of the tool) is easily identified whereas the other two components evolve as sinusoidal signals. The sum of these two components, located in the xy-plane, can be decomposed into radial F_r and tangential F_t (with respect to the tool displacement) components, which are more physical quantities.

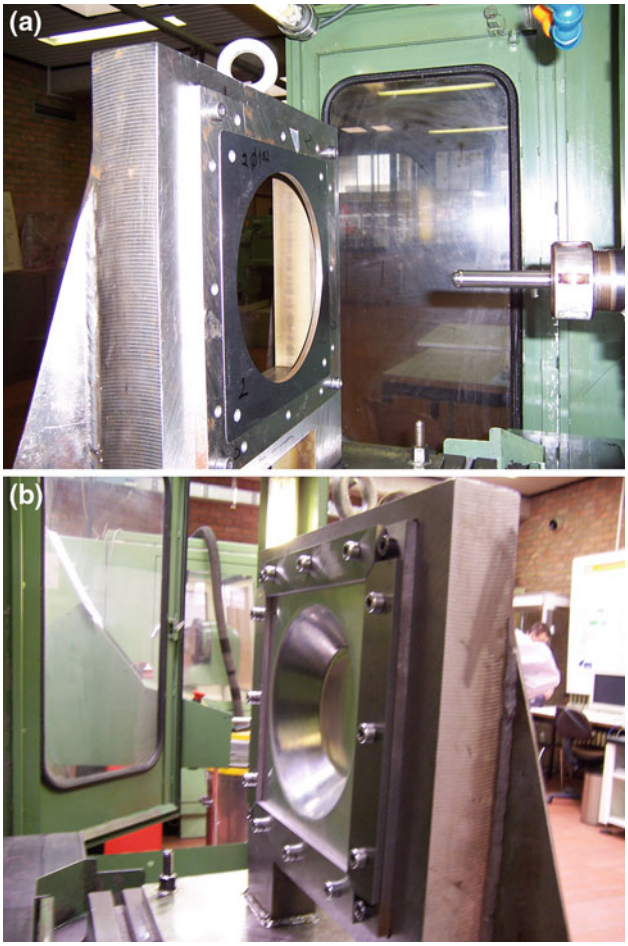

Fig. 5 Experimental SPIF device (picture courtesy of Johan VERBERT, KUL). **a** Close-up view of backing plate and tool. **b** Side view of the complete clamping system

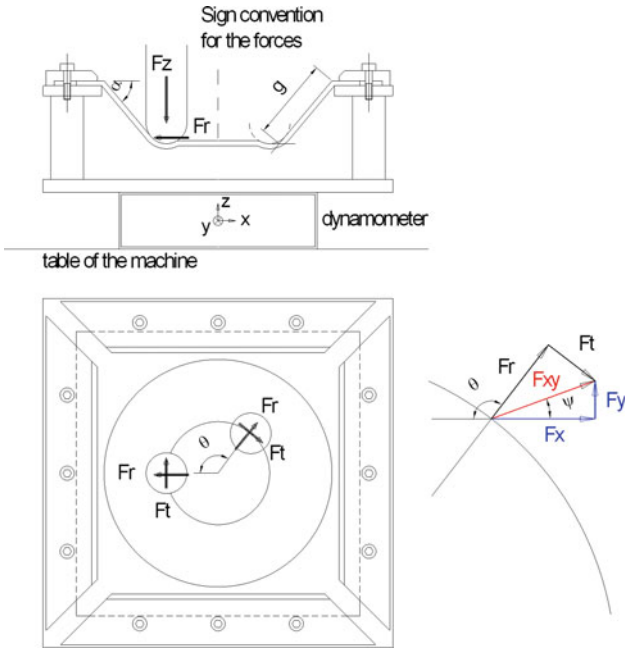

Fig. 6 Definition of SPIF axial, radial and tangential force components [8]

In addition to force measurements, Digital Image Correlation Technique was also used to measure the forming of the 20° cone. The analysis of the FEM predictions in terms of displacements and strains can be found in [25].

2.2 Parts' geometries

Two cones have been studied. Their geometries and the SPIF parameters are summarized in Table 1.

The scallop height Δh is related to the depth increment Δz, the tool diameter d_t and the wall angle α [8]:

$$\Delta z = 2 \sin\alpha \sqrt{\Delta h \cdot (d_t - \Delta h)}. \quad (1)$$

It is more convenient to use the scallop height as a process characteristic parameter than the depth increment since the scallop height is more closely linked to surface quality.

Table 1 Cone geometry and SPIF parameters

Cone geometry and SPIF parameters	Cone 20	Cone 60
Cone diameter	150 mm	150 mm
Initial sheet thickness t	1.2 mm	1.2 mm
Wall angle α (see Fig. 3)	20°	60°
Number of contours (see Fig. 2)	45	50
Scallop height Δh (see Fig. 7)	15.0 μm	18.5 μm
Depth increment between contours Δz (see Fig. 7)	0.2647 mm	0.7440 mm
Tool diameter d_t	10 mm	10 mm

2.3 Material and analytical force prediction

The material used was a soft Al–Mn–Fe aluminum alloy in fully annealed state: AA3003-O, supplied by Corus. The initial thickness of the metal sheet was 1.2 mm. When forming a cone with this material and thickness, the maximum wall angle that can be achieved before failure is around 71° [26]. Its ultimate tensile strength (R_m) is 103 N/mm^2.

The axial force F_z in steady state can be predicted by the experimental parameters: the tensile strength R_m, the sheet thickness t, the tool diameter d_t, the scallop height Δh and the wall angle α following the formula established by Aerens et al. [8]:

$$F_z = 0.0716 \cdot R_m \cdot t^{1.57} \cdot d_t^{0.41} \cdot \Delta h^{0.09} \cdot \alpha \cdot \cos\alpha \quad (2)$$

with F_z in N, R_m in N/mm^2, t, d_t and Δh in mm and α in degrees.

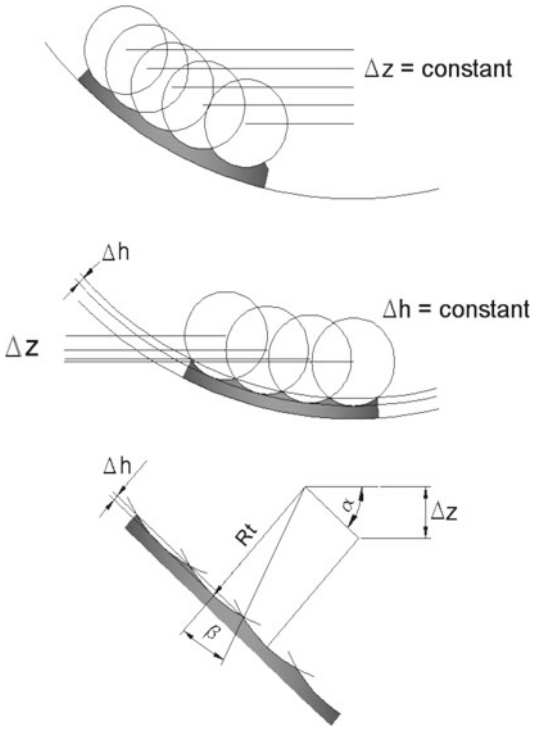

Fig. 7 The scallop height Δh versus the depth increment Δz [8]

For the cones with 20° and 60° wall angles, Eq. 2 gives axial force predictions F_z equal to 325 and 529 N, respectively. These values match the experimental forces with a high degree of confidence, as shown by Fig. 17 (showing the total force F_{tot} of the 20° cone, which can be transformed into axial force knowing the $F_z/F_{tot} = 0.97$, according to Table 5) and 19 (showing the axial force F_z of the 60°cone).

3 Finite elements simulations

Two finite element codes were applied and compared. The first one was Lagamine, a research code developed since 1980 at the university of Liege [27]. It contains a huge variety of element types and material model and has been used successfully for years for material forming applications. In addition, it could easily be customized for SPIF simulations since the source code was available.

The second FE code was the implicit version of Abaqus (Abaqus/Standard v. 6.5-4). This was used as a reference for validation purposes.

3.1 Lagamine model

The Lagamine code uses a Lagrangian approach taking into account large strains and displacements. The following elements are used:

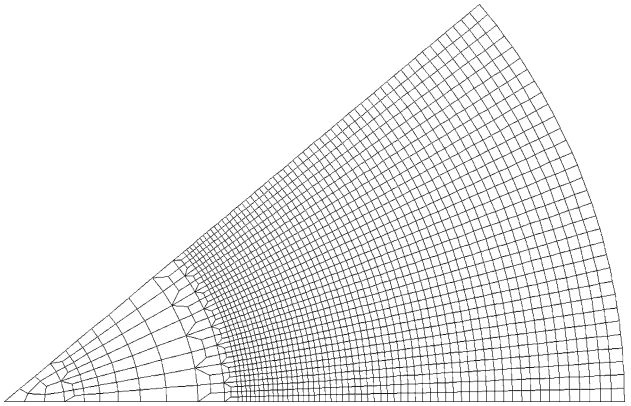

Fig. 8 Shell Lagamine mesh used for the 40° pie simulations of the 20° and 60° cone (Lagamine pie model)

- the **solid element BWD3D** is an 8-node 3D brick element with a mixed formulation adapted to large strains and large displacements with only one integration point and an hourglass control technique. It applies methods proposed by Wang and Wagoner [28] to prevent shear locking and volumetric locking, associated with a co-rotational reference system. Its description can be found in Duchêne's article published in 2007 [29];
- the **contact element CFI3D** [30] is coupled with the BWD3D solid element. It checks the contact at the surface integration points of the metal sheet with the spherical tool, which is assumed to be rigid (i.e., non-deformable). It assesses pressure based on a penalty approach and friction as predicted by Coulomb's friction law. It computes contact nodal forces used to search for equilibrium. An adapted version is used for the shell element COQJ4.
- the **shell element COQJ4** [31] is a 3D quadrilateral element with four nodes. Owing to the developments of Jaameil et al. [32], it is based on Marguerre's shallow shell theory. The global behavior of the element can be divided into two modes. On the one hand, its bending behavior is based on the classic discrete Kirchhoff theory (DKT) and uses a bi-cubic interpolation. On the other hand, the membrane behavior uses a bi-quadratic interpolation.

The Lagamine code was used in a first step to simulate a line test, which presents a deformation mechanism close to SPIF [33–35]. This study generated a sensitivity analysis of the force prediction to the element type, the material law parameters and the identification method of these parameters. Its results are summarized briefly in Sect. 4 to justify why only certain constitutive models and sets of parameters were applied to predict SPIF forces.

The Lagamine simulations used to predict the tool force in the 20° and 60° cones processed by SPIF were done only with shell elements. The mesh used is presented in Fig. 8.

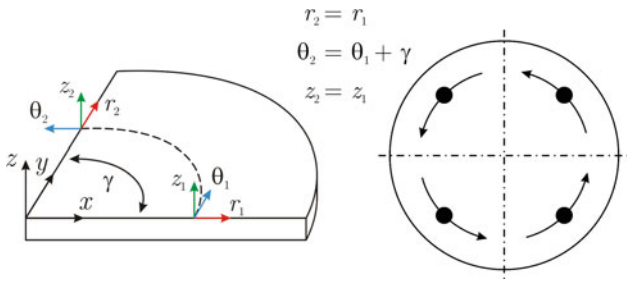

Fig. 9 Rotational boundary conditions and their virtual tools (schematic view of a 90° pie)

In order to minimize the impact of the material missing at both edges of the pie, rotational (or cyclic symmetry) boundary conditions were imposed, which consist of a link between the displacements of both edges, as presented schematically in Fig. 9. The reason for this improvement is that the rotational boundary conditions do not prevent the material at the edges of the pie mesh from being carried along in the tangential direction of the tool movement. Indeed, even without friction between the tool and the metal sheet, the tool induces a force component in the tangential direction of the tool displacement because of the material that surrounds the tool during its movement. Since the tool always moves in the same tangential direction, the whole cone has a small tendency to twist around its axis of rotational symmetry, a movement that can be simulated with these boundary conditions even at the edges of the pie, but not with the symmetry boundary conditions. Even though these conditions do not exactly reproduce the missing material, they induce a smaller deviation from experimental displacement observations at the pie edges than symmetry boundary conditions [36], whereas both lead to similarly accurate results far from the edges towards the center of the pie.

3.2 First-order brick element model and submodel of Abaqus

In all the Abaqus models, the sheet is composed of three layers of first-order, eight-node brick elements with reduced integration (C3D8R). For the elements at the pie-tip, wedge-shaped elements (6 nodes) of first order and with reduced integration are used. The forming tool is modeled as an analytical rigid sphere, with a rigid body translation according to the experimental tool path. The contact definition is "hard", i.e., the nodes on the contact surface of the sheet are not allowed to penetrate the analytical rigid body of the tool. A Coulomb tool-sheet frictional contact behavior is adopted, with a friction coefficient equal to 0.05.

Two different models were employed with different meshes, as shown in Fig. 10. In the 40° pie model (see Fig. 10a), symmetry boundary conditions were applied on

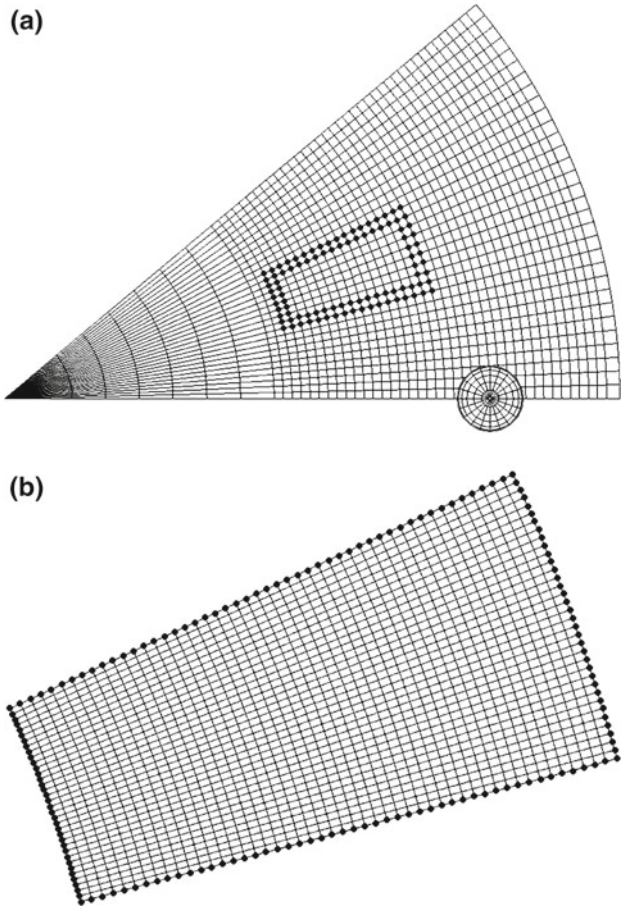

Fig. 10 Brick Abaqus meshes used for simulations of the 20° and 60° cone. **a** 40° pie model. **b** Submodel

the 0°- and 40°-sections. The nodes on the outer circular edge and in contact with the backing plate were fixed to model the sheet clamping. The Abaqus submodel had a much finer mesh and a smaller part of the sheet was modeled compared to the pie-model with brick elements (Fig. 10b). The boundary conditions on the four edges of the submodel (shown in bold in Fig. 10a and b) are imposed to be equal to the nodal displacements of the Abaqus pie model. This was accomplished through linear interpolation (in space and in time) of the nodes of the pie model shown in bold in Fig. 10a, which had been saved for each time step. The "submodeling" option in the Abaqus software allows this procedure to be done in an automated way. As shown in Fig. 10, the submodel was located around the center of the pie model in order to avoid edge effects of the non-physical symmetry boundary conditions imposed on the latter. This submodeling strategy has also been followed in Eyckens et al. [37,38] and Aerens et al. [8]. In the latter article, a more detailed description can be found for the same process parameters.

3.3 Constitutive laws

Due to the choice of material, the static loading and the room temperature, an elastic–plastic behavior law seemed to be the most suitable. The elastic range is described by Hooke's law where the Young's modulus $E = 72,600$ MPa and the Poisson's ratio $\nu = 0.36$ were identified using an acoustic method.

The isotropic von Mises yield locus as well as the anisotropic Hill yield loci have been taken into account, in order to show the effect of the sheet anisotropy on the force predictions. The experimental Lankford coefficients, r_0, r_{45} and r_{90} at 0°, 45° and 90° from the rolling direction, are equal to 0.68, 0.73 and 0.66, respectively. We assume that the laminated sheet remains orthotropic during the deformation, whereas the orthotropy axes may be subjected to a time-dependent rotation $\underline{\underline{R}}$. This rotation is either derived from the polar decomposition of the deformation gradient, or defined by the evolution equation $\dot{\underline{\underline{R}}} = \underline{\underline{\Omega}} \cdot \underline{\underline{R}}$ where $\underline{\underline{\Omega}}$ is the total spin, i.e., the antisymmetric component of the velocity gradient. We take the form of Hill's quadratic yield function:

$$F_{Hill}(\underline{\underline{\sigma}}) = \frac{1}{2}\Big[(H+G)\sigma_{11}^2 + (H+F)\sigma_{22}^2 - 2H\sigma_{11}\sigma_{22} + 2N\sigma_{12}^2\Big] - \sigma_F^2 = 0 \tag{3}$$

where the parameters F, G and H are defined using the following relations:

$$F = \frac{2r_0}{r_{90}(1+r_0)}, \quad G = \frac{2}{(1+r_0)}, \quad H = \frac{2r_0}{(1+r_0)}.$$

The N parameter was simultaneously fitted by an inverse method with the hardening parameters as presented in Sect. 4.

$\underline{\underline{\sigma}}$ is the Cauchy stress tensor, whose components are defined assuming that direction 1 is the sheet RD, 2 is the transverse direction (TD) and 3 the normal direction.

Various hardening models were used:

- an **isotropic Swift hardening law** (no saturation):

$$\sigma_F = K\left(\epsilon_0 + \epsilon^p\right)^n. \tag{4}$$

  The material parameters ϵ_0, K and n were identified using a single test (either a uniaxial tension or simple shear test) or preferably by using the averages of the stress–strain curves obtained by such tests at various orientations with respect to the rolling direction. The initial value of the yield stress is given by the relation $\sigma_0 = K\epsilon_0^n$. Swift's law is adequate to describe the behavior of materials which exhibit non-saturated isotropic hardening, but very weak or negligible kinematic hardening.
- an **isotropic Voce hardening law** (saturation):

$$\sigma_F = \sigma_0 + K\left(1 - e^{-n\cdot\epsilon^p}\right), \tag{5}$$

  where ϵ^p is the plastic strain, and K, σ_0, and n are the material parameters.
- a **kinematic Armstrong–Fredericks law**, coupled with one of the previous isotropic hardening models (a mixed hardening law is used, instead of a purely kinematic one). The stress tensor $\underline{\underline{\sigma}}$ is replaced by $\underline{\underline{\sigma}} - \underline{\underline{X}}$ where $\underline{\underline{X}}$ is the back-stress. The material is assumed to have the same behavior under tension and compression at the beginning of the process, the evolution of the back stress being described by a saturation law thoroughly investigated by Lemaître and Chaboche [39]:

$$\overset{\nabla}{\underline{\underline{X}}} = C_X\left(X_{sat}\,\dot{\underline{\underline{\epsilon}}}^p - \underline{\underline{X}}\,\dot{\epsilon}^p\right), \tag{6}$$

  where $\overset{\nabla}{\underline{\underline{X}}}$ is Jaumann's objective derivative applied on the back-stress, X_{sat} characterizes the saturation value of the kinematic hardening, and the material parameter C_X characterizes the rate of approaching saturation and $\dot{\epsilon}^p$ is the anisotropic equivalent plastic strain rate for Hill or the isotropic one for Von Mises.
- a **kinematic Ziegler law**:

$$\overset{\nabla}{\underline{\underline{X}}} = C_A\frac{1}{\sigma_F}\left(\underline{\underline{\sigma}} - \underline{\underline{X}}\right)\dot{\epsilon}^p - G_A\,\underline{\underline{X}}\,\dot{\epsilon}^p, \tag{7}$$

  where C_A is the initial kinematic hardening modulus and G_A is the rate at which the kinematic hardening modulus decreases with increasing plastic deformation. Both kinematic hardening models are available in Lagamine but only Ziegler's was available in the version of Abaqus used.

4 Identification of the material parameters

4.1 Introduction

An inverse method was used to fit the material data. This method, coupled with a FE code, can be used to determine the material parameters of a complex material law. The principle of this method is to choose a set of tests, whose results are sensitive to the material data to adjust. These tests are simulated using an initial set of data, chosen arbitrarily—the better this initial guess, the faster the method. Then, the numerical results are compared with the experimental measurements, and the non-linear least-squares problem is solved using a Levenberg Marquardt minimization algorithm [40]. The material data are adjusted iteratively until the difference between the numerical and experimental curves is minimized. The advantage of this method is the possibility of choosing non homogeneous tests to fit the parameters, thereby inducing heterogeneous stress and strain states close to the ones reached during the process to be simulated.

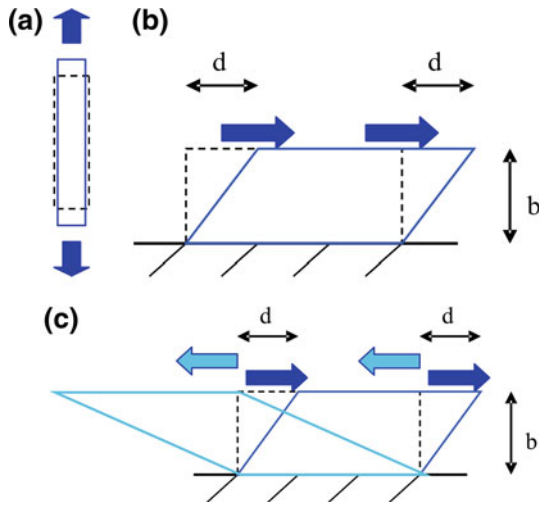

Fig. 11 Description of the classic tests: **a** tensile, **b** shear and **c** Bauschinger tests

Figure 11 shows the so-called classic tests. Unlike these, the line test, presented in Fig. 12, is an additional test chosen because its stress and strain states are similar to the ones occurring during SPIF. Indeed, this test shows localized strain gradients and through-thickness shear that do not occur in classic tests. The square sheet had a thickness of 1.5 mm and the spherical tool radius was 5 mm. The tests were performed three times and the bolts of the frame were tightened using the same torque value. This point is essential for ensuring a repeatability of the test results. The displacement of the tool was composed of five steps with an initial position tangent to the top surface of the sheet: a first indent of 5 mm (step 1), a line movement at the same depth along the x-axis (step 2), then a second indent up to a depth of 10 mm (step 3) followed by a line at the same depth along the x-axis (step 4) and by unloading (step 5).

Only the first step of this test was used during the inverse method procedure to determine accurate material data. However, the whole test was used as an experimental validation as it is sensitive to kinematic hardening.

Table 2 presents the nine sets of material parameters identified in this study and detailed in the next sections. Some of these will not be used for the cone simulations but only on the line test simulations discussed hereafter.

For the Abaqus simulations, the Swift parameters of Sets 1, 1* and 2 were chosen to be different from the ones used for the Lagamine simulations and shown in Table 2: $K = 183\,\text{MPa}$, $\epsilon_0 = 1.49 \cdot 10^{-3}$ MPa and $n = 0.222$. Nevertheless, the respective flow curves do not deviate more than 4 MPa for $\epsilon^p < 100\%$.

4.2 Material parameter sets 1 and 2

The tests described in Fig. 11 were used to determine the material data. As these tests are assumed to be homogeneous (this have been verified using Digital Image Correlation), only an analytical adjustment was performed using the relations (3–7) and the usual correlations between Lankford coefficients and the Hill material parameters, except for N, which was improved using the inverse method. The type of element (brick or shell) does not affect these parameters, which are assumed to be the true material parameters.

For Set 1, the Swift isotropic hardening law was coupled with Armstrong–Frederick's kinematic hardening and Hill's yield locus. However, the optimizer provided a set of parameters where both C_X and X_{sat} were equal to zero, indicating an optimal solution without kinematic hardening. The good correlation between the experimental and simulation results can be checked in a paper published by Bouffioux [35]. Only a small number of validations will be presented in this section. Set 1* was derived from Set 1 and was not obtained using inverse modeling. Its sole purpose was to check the effect of taking into account the anisotropic Hill yield locus, in comparison with the isotropic Von Mises one for an identical hardening model (see Fig. 17 for the 20° cone).

For Set 2, the von Mises yield locus was coupled with Ziegler hardening, available in both Abaqus and Lagamine. Unlike for Set 1, the optimizer converged towards a set of parameters containing a significant amount of kinematic hardening. In addition, this set provides a good prediction of experimental results, except for the tensile test. The Bauschinger test in Fig. 11 could indicate that kinematic hardening happens. A second confirmation was provided through the simulations of the whole line test, using brick elements and the Lagamine code with Set 1* and Set 2, which were then compared (see Fig. 13) with experimental results. The brick simulation prediction with Set 2 is slightly closer to the experimental measurements, giving a possible indication of the usefulness of kinematic hardening.

However, with both laws, the gap between the simulation and the experimental measurement was still so large that either these material parameters are incorrect or else the type of finite element, the material law or the mesh density is not able to model the material flow accurately. In order to find an answer to this delicate question, the sensitivity of the line test in relation to the following simulation parameters, either numerical or physical, was evaluated using brick elements: in-plane mesh density with a fixed number of layers across the thickness (i.e., 3 layers), inaccuracy in the thickness measurement, defect of flatness of the sheet, slipping of the sheet in its blank-holder, rigidity of the machine, geometry of the tool, or friction with the tool. None of these parameters could have a significant enough influence so as to explain the large difference between the experiments and the simulation, as shown by Bouffioux et al. [35].

Since neither of these two material parameter sets seemed to be able to capture the actual material behavior during the

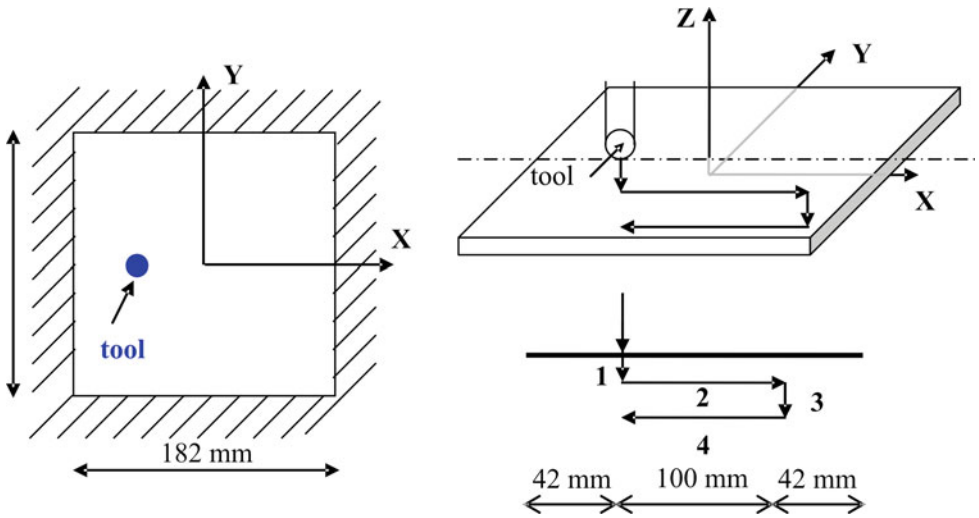

Fig. 12 Description of the line test

Table 2 Parameters of the material laws used in line test and cone simulations (K, C_A, X_{sat}, and σ_0 in MPa)

Set number	Name and hardening type	Yield surface coefficients	Swift/Voce parameters	Back-stress data
Set 1	Hill/Swift	$F = 1.224$, $G = 1.193$, $H = 0.8067$	$K = 183$, $n = 0.229$,	$C_X = 0$
	Isotropic hardening	$N = L = M = 4.06$	$\epsilon_0 = 0.57{\cdot}10^{-3}$	$X_{sat} = 0$
Set 1*	Von Mises/Swift	$F = G = H = 1$	$K = 183$, $n = 0.229$	$C_X = 0$
	Isotropic hardening	$N = L = M = 3$	$\epsilon_0 = 0.57{\cdot}10^{-3}$	$X_{sat} = 0$
Set 2	Von Mises/Swift	$F = G = H = 1$	$K = 146.7$, $n = 0.229$	$C_A = 240.6$
	Ziegler (kine. hard)	$N = L = M = 3$	$\epsilon_0 = 1.5 \cdot 10^{-3}$	$G_A = 11.2$
Set 4	Von Mises/Swift	$F = G = H = 1$	$K = 175$, $n = 0.328$	$C_A = 800$
Bricks	Ziegler (kine. hard)	$N = L = M = 3$	$\epsilon_0 = 0.15 \cdot 10^{-3}$	$G_A = 45.9$
Set 5	Hill/Swift	$F = 1.224$, $G = 1.193$, $H = 0.8067$	$K = 111$, $n = 0.266$	$C_X = 51.4$
Shells	Arm-Fred (kine. hard)	$N = L = M = 4.06$	$\epsilon_0 = 0.5 \cdot 10^{-3}$	$X_{sat} = 46$
Set 5*	Von Mises/Swift	$F = G = H = 1$	$K = 111$, $n = 0.266$	$C_X = 51.4$
Shells	Arm-Fred (kine. hard)	$N = L = M = 3$	$\epsilon_0 = 0.5 \cdot 10^{-3}$	$X_{sat} = 46$
Set 6	Von Mises/Swift	$F = G = H = 1$	$K = 94$, $n = 0.266$	$C_A = 3{,}000$
Shells	Ziegler (kine. hard)	$N = L = M = 3$	$\epsilon_0 = 0.083 \cdot 10^{-3}$	$G_A = 56.9$
Set 7	Von Mises/Voce	$F = G = H = 1$	$K = 109$, $n = 21$	$C_A = 0$
Bricks	Isotropic hardening	$N = L = M = 3$	$\sigma_0 = 15$	$G_A = 0$
Set 8	Von Mises/Voce	$F = G = H = 1$	$K = 89$, $n = 22.5$	$C_A = 83$
Bricks	Ziegler (kine. hard)	$N = L = M = 3$	$\sigma_0 = 20$	$G_A = 0$

line test, a different approach was required and a new identification method was developed.

4.3 Material parameter sets 4, 5, and 6

For these sets, a new identification procedure was used. It consists in applying the inverse method coupled with FE simulations (Fig. 14) of both a tensile test and a simple indent test (i.e., step 1 of the line test shown in Fig. 12). The line test, performed with the SPIF set-up, contains heterogeneous stress and strain fields with tension, compression and shear stresses. The material parameters obtained were expected to be more accurate, since these heterogeneous stress and strain fields are also present in the SPIF process.

Indeed, the data adjusted by such a method gave a better prediction of the global material behavior when looking at the line test simulation results (Fig. 15). However, the notion of "true material parameter" is not accurate as

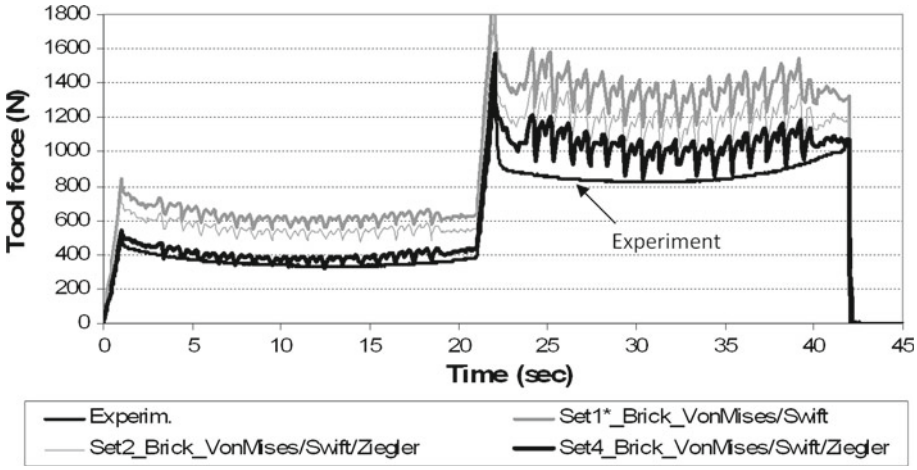

Fig. 13 Experimental and predicted (Set 1*, 2, 4) force–displacement curves for the line test

performing exactly the same identification with brick or shell elements (Set 4 Brick and Set 6 Shell) generated different sets of material data. Another way to see this effect is to compare the predictions of Set 4 used with shell elements or brick elements in Fig. 15. Apparently, the phenomenological constitutive models used with a given mesh and contact model do not make it possible to obtain a unique set of material data. The inaccuracy of the FE simulations (due to overly coarse meshes, elements not able to model actual behavior within the thickness, or an inaccurate rheological model) can be corrected by using well-chosen material data, which thereby lose some of their physical meaning.

The predictions based on Sets 2 and 4 differ only in their identification method. The improved simulation results of Set 4 Brick (not only for step 1 of the line test for which it was identified but for the whole test) confirm the interest of this new identification procedure.

Simulations performed with shell elements (with five integration points across the thickness) seem to provide a slightly better modeling of the bending state occurring in the line test than the ones performed with three layers of brick elements. However, the through-thickness shear cannot be taken into account by these shell elements and the results from the 20° and 60° cones will show the limitations of using such elements (see e.g. Figs. 17 and 20).

Finally, note that the brick element C3D8R of Abaqus supplies a remedy for the shear locking problem, but the rank-deficiency of the stiffness matrix may produce spurious singular (hourglassing) modes, which can often make the elements unusable, unless it remains under control [41].

4.4 Material parameter sets 7 and 8

The line, tensile and shear tests do not reach sufficiently large strains to clearly decide whether or not a Voce law (with saturation of isotropic hardening) is preferable to a Swift law (with strictly increasing hardening). However, the analysis of

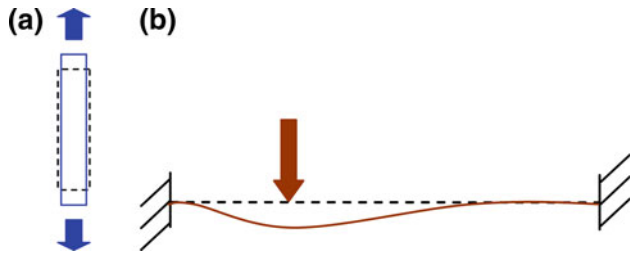

Fig. 14 Description of the tests chosen for the second method of data identification: **a** tensile test, **b** indent test

the usual stationary force level reached in all the SPIF experiments [8,13,22] suggests that a Voce law is more adapted to the large deformation behavior of the studied aluminum sheet. In particular, the links that can be established between the Kocks and Mecking dislocation-based hardening models [42] and the phenomenological Voce model are in favor of this saturation model for very large strains.

For these two sets of material parameters, the identification method consisted in fitting material data using a tensile test (with a maximal experimental equivalent strain of 0.335), a monotonic shear test (with a maximal experimental equivalent strain of 0.431), two Bauschinger shear tests (using two different levels of pre-strain Gamma $= d/b = 10$ and 30%, as illustrated in Fig. 11) and a simple indent test. As this hardening model was not available with Lagamine's shell element, only the set of material data of the brick elements is provided.

Figure 16 compares the evolution of the predicted force with a Swift or Voce law with the experimental values. At this stage, given the relatively small level of deformation reached during these simple tests, the Voce law does not seem to be more accurate than the Swift law. Indeed, the predictions with Set 6, which uses a Swift law, are more accurate than the other ones but this is probably due to the fact that this simulation was performed with shell elements. However, it will be shown later, with the cone simulations, that the Voce law is more adapted when larger deformations take place.

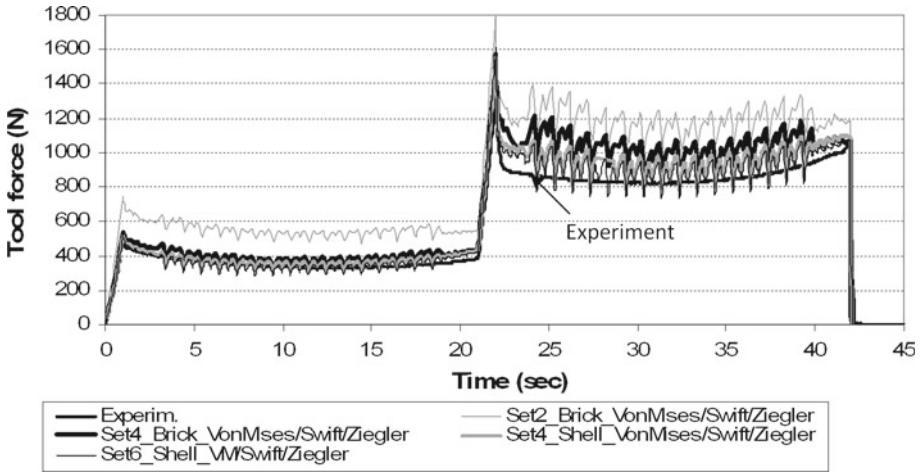

Fig. 15 Experimental and predicted force–displacement curves for the line test (with Set 2, Set 4 Brick and Shell, and Set 6)

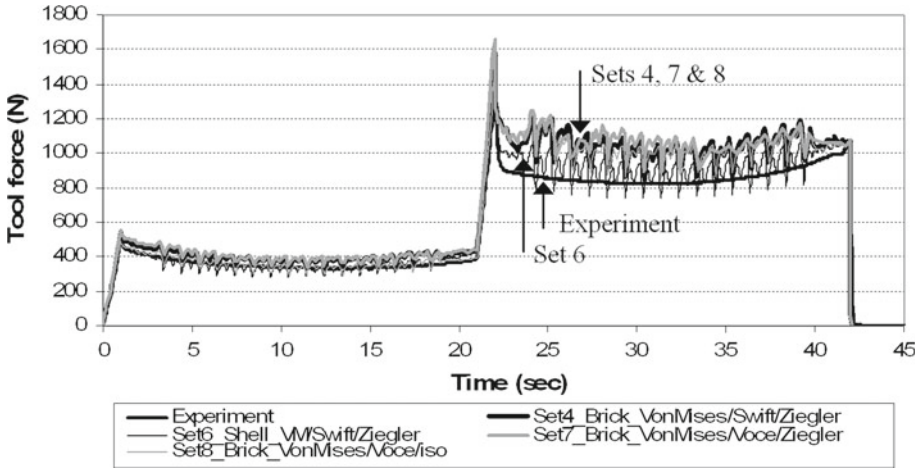

Fig. 16 Experimental and predicted force–displacement curves for the line test (with Sets 4, 6, 7, and 8)

4.5 Conclusion about the identification procedures

The line test simulation results lead us to the conclusions that the second parameter identification method is preferable to the first one. In addition, the presence of large strain in SPIF process justifies the use of a third method.

Finally, these simulations proved that the choice of the material parameter set cannot be made separately from that of the element type and the simulations to be performed.

5 Force results in cone simulations

5.1 Introduction

When modeling Single Point Incremental Forming, obtaining accurate force predictions is always a difficult task. In order to evaluate the influence of various material models and of the elements used, 10 simulations were performed.

Two different FE codes were used: Lagamine with shell elements and Abaqus with brick elements, using two different mesh densities (see Figs. 8 and 10). Unlike during the experimental tests, no tool rotation was imposed in the FE simulations but only a rigid body displacement according to the experimental tool path. A Coulomb friction coefficient of 0.05 was used in all simulations, except those shown in Fig. 24 since they were used to evaluate the influence of friction. The characteristics of those 10 simulations are summarized in Table 3.

When interpreting the FE force predictions, an essential difference between shell (Lagamine) and brick (Abaqus) FE simulations should be kept in mind. Brick elements are allowed to shear (plastically) in a plane containing the sheet thickness direction. Indeed, as shown by Table 4, which gives the values of the through-thickness shear angles for several simulations, such a shear does take place, especially for the larger wall angle of 60°. The shear angle values were computed using the final position vector from a node on the outer cone surface towards the corresponding node on the inner surface and expressing it in the local reference frame 1-2-3 attached to the outer sheet surface. For this frame, the third axis is aligned with the local sheet normal direction (see

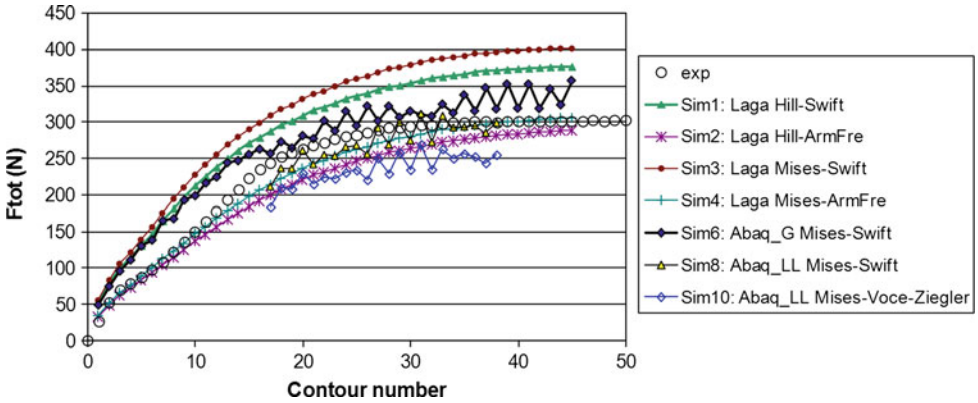

Fig. 17 Total force for the 20° cone simulations

Table 3 Characteristics of FEM simulations

Name	FE code	Model	Yield locus	Isotropic hardening	Kinematic hardening	Parameter set and element
Sim1	Lagamine	Global	Hill	Swift	–	Set 1 Shell
Sim2	Lagamine	Global	Hill	Swift	Arm.-Frederick	Set 5 Shell
Sim3	Lagamine	Global	Von Mises	Swift	–	Set 1* Shell
Sim4	Lagamine	Global	Von Mises	Swift	Arm.-Frederick	Set 5* Shell
Sim5	Lagamine	Global	Von Mises	Swift	Ziegler	Set 6 Shell
Sim6	Abaqus	Global	Von Mises	Swift	–	Set 1* Brick
Sim7	Abaqus	Global	Von Mises	Voce	Ziegler	Set 8 Brick
Sim8	Abaqus	Submodel	Von Mises	Swift	–	Set 1* Brick
Sim9	Abaqus	Submodel	Von Mises	Voce	–	Set 7 Brick
Sim10	Abaqus	Submodel	Von Mises	Voce	Ziegler	Set 8 Brick

Table 4 Through-thickness shear angles γ_{13} and γ_{23} obtained with brick (Abaqus) simulations of the 20° and 60° cones

Name	Model	Yield locus	Isotropic hardening	Kinematic hardening	Cone 20°		Cone 60°	
					γ_{13}	γ_{23}	γ_{13}	γ_{23}
Sim6	Global	Von Mises	Swift	–	0°	1°	−13°	5°
Sim7	Global	Von Mises	Voce	Ziegler	–	–	−11°	1°
Sim8	Submodel	Von Mises	Swift	–	0°	3°	−16°	18°
Sim9	Submodel	Von Mises	Voce	–	–	–	−19°	17°
Sim10	Submodel	Von Mises	Voce	Ziegler	1°	3°	−7°	9°

The negative values of γ_{13} correspond to the sketch in Fig. 3

Fig. 3). The exact calculation method of the corresponding unit vectors is given in Eyckens et al. [25]. The angles given in Table 4 are the average values of nine such position vectors, located in the center of the submodel mesh (see Sect. 3.2), i.e., at a distance of about 55 mm from the pie model's tip in the undeformed configuration.

It can be noted in Table 4 that for the 20° cone, through-thickness shear is practically absent. For the 60° cone, however, it is significant and dependent on the mesh density used (compare Sim6 to Sim8 and Sim7 to Sim10). A dependence on the material model used can also be seen by comparing Sim7 to Sim6 and Sim10 to Sim8 or Sim9: the use of kinematic hardening appears to reduce the total through-thickness shear prediction, at least for 60° cone.

In the following discussion, the force components will always be given as an average per contour. This average is computed, for each contour separately, for the time interval during which the tool angular position is within the central third part of the respective mesh, in order to avoid edge effects due to the boundary conditions.

In addition, it has been verified in Henrard's PhD thesis [43] that the results of a 360° (whole blank), 90° (one quarter of the blank) and 45° (one eight of the blank) simulations produce very similar results. In particular, the maximum

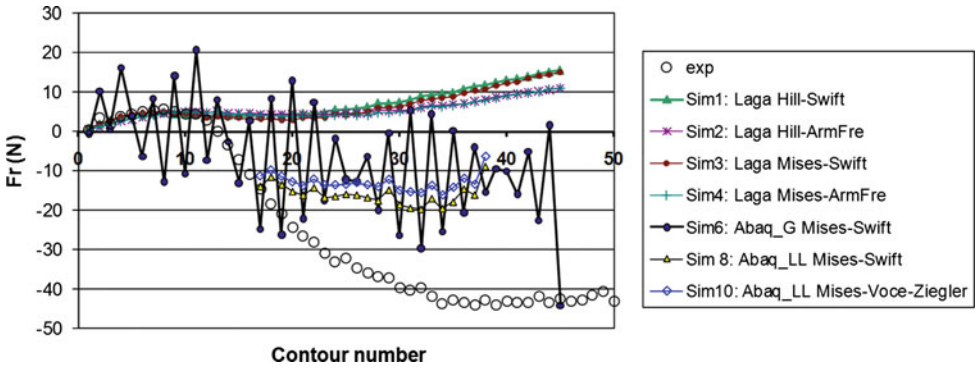

Fig. 18 Radial force for the 20° cone simulations

relative error of the partial simulations with respect to the full one was, for the axial force F_z, smaller than 10%.

Comparing the respective ratios between the different stabilized force components is an additional way of detecting the strong differences in material flow happening in the 20° and 60° cones. First, the axial force is in both cases the main component and it is the most important one for the validation of the simulations. Then, the radial force level strongly depends on the wall angle: this component varies both in terms of magnitude and direction, as will be proved later. Finally, the tangential force is directly related to the friction and contact characteristics. During the experimental tests, the tool's rotation speed was chosen to be proportional to the tool's linear speed in such a way that there would be a point of its surface with a rolling contact. Since the contact zone is approximately a line, as shown by Eyckens [38], two distinct zones appear: one with local relative tool velocity in the same direction as the tool movement, and the other one opposite to the tool movement. These two zones either (partly) compensate each other or not, depending on the wall angle. The FE models, which neither take the tool rotation into account nor have an accurate contact zone due to overly coarse meshes (even for the submodel), cannot accurately predict this phenomenon. For this reason, one cannot expect accurate predictions of tangential force values F_t.

5.2 FE force predictions for the 20-degree cone

The evolution of the experimental and predicted (7 simulations) total tool force is shown in Fig. 17 for the 20° cone. One can observe the following regarding force predictions:

- The effect of anisotropy can be estimated through the comparison of the results from `Sim1` and `Sim3` using isotropic hardening or `Sim2` and `Sim4` using mixed hardening. This effect is relatively small. This can be explained by two causes: firstly, the Lankford coefficients show a weak planar anisotropy, and secondly, the use of a pie model (with the Rollind Direction (RD) aligned with the x-axis as shown in Fig. 8) is not a reliable approach to check the overall variation due to anisotropy. However, a global 360° simulation did not highlight strong sinusoidal variations of the predicted force during one contour, and the average force per contour predicted using a Hill anisotropic material model showed very similar results to the one predicted with an isotropic Von Mises model [43].
- `Sim1`, `Sim3`, and `Sim6` using Swift isotropic hardening with either shell or brick elements produced poor results. The use of a brick submodel, having a more refined mesh (`Sim8` and `Sim10`), seems to improve the prediction significantly. This could suggest that even for a wall angle as low as 20°, which does not show significant through-thickness shear (as shown in Table 4), the reduced integration elements are very sensitive to mesh density. Finer meshes coupled with better hardening model bring the predictions closer to the converged solution.
- `Sim6`, `Sim8`, and `Sim10`, performed with Abaqus's brick element, display more oscillations than the other four simulations performed with Lagamine's shell element, even though their mesh densities are similar. Lagamine's shell element has four in-plane integration points and for each of them, the stress gradient was integrated using five integration points across the thickness. Its associated contact element checks the contact state and computes the contact pressure at four integration points located at the element's surface. Lagamine's nodal forces are then energetically equivalent to any contact happening on the surface layer. Abaqus, on the other hand, merely computes a contact force at each surface node and has only three integration points (both for the pie model and the submodel) across the thickness (three layers of reduced-integration elements having each just one integration point).
- Even though they use the same law, `Sim8` proved more accurate than `Sim6`. With the submodel technique, the same number of elements is used across the thickness, but the in-plane mesh is much more refined compared to the Abaqus and Lagamine pie model meshes. Therefore, it can make a much better prediction of the localized

Table 5 Experimental stabilized absolute and relative force components for cone 20° and 60°

	F_r [N]	F_r/F_{tot}	F_t [N]	F_t/F_{tot}	F_z [N]	F_z/F_{tot}	F_{tot} [N]
Cone 20	−42.00	−0.14	57.00	0.19	293.00	0.97	302.00
Cone 60	203.00	0.35	100.00	0.17	530.00	0.92	576.00

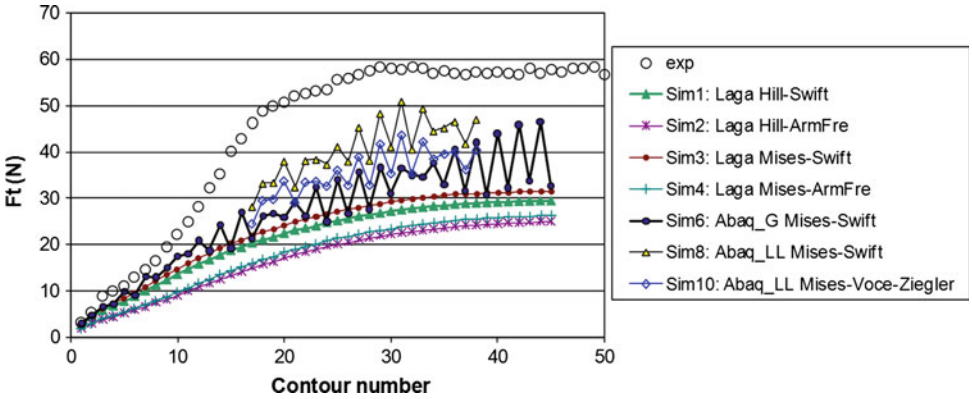

Fig. 19 Tangential force for the 20° cone simulations

plastic zone around the tool contact zone, as illustrated in Eyckens's paper [38].

– `Sim2` and `Sim4`, which both use Armstrong–Frederick's kinematic hardening law, predicted more accurate forces than did `Sim1` and `Sim3`, using Swift isotropic hardening for shell elements. The experimental stationary value is almost perfectly predicted by `Sim2` and `Sim4`. Note that the analytical formula given by Eq. 2 predicted a quite accurate value of 325 N.
– `Sim10` is less accurate than `Sim8`. The underestimation of F_z may be due to the apparent underfitting of the uniaxial tensile test in the identification procedure. Note that in the wall of the 20° cone, accumulated plastic strains up to about 30% are reached, which is not higher than the level reached during the tests used in the identification procedure. It appears that with the material laws currently used, the line test (featuring bending of the sheet) and the tensile test cannot be accurately captured with the same material parameters. Increasing the number of elements across the thickness (three layers) in the model used during the identification would likely improve the bending state prediction and increase the accuracy of the results even more.

Clearly, the use of a kinematic hardening law combined with a saturating isotropic Voce hardening is one way of reducing the predicted vertical tool force and bringing it closer to experimental measurements. Another one is the use of the submodeling technique, which likewise decreases the global force level and yields to accurate force predictions even without kinematic hardening. Both brick and shell elements provide accurate results for this small wall angle cone geometry because the through-thickness shear remains limited (as illustrated by Fig. 4 and Table 4).

Note that the total force is mainly due to the axial force, as shown in Table 5 (F_z/F_{tot} equals 0.97). The experimental and predicted radial force values, shown in Fig. 18, are significantly lower as F_r/F_{tot} is limited to 0.14. The predicted radial force depends more on the choice of element and mesh refinement than on the constitutive law.

For the first contours (1–10), experimental and numerical forces computed using shell elements were very accurate, regardless of the constitutive laws (`Sim1` to `4`). On the other hand, the value predicted using brick elements presented strong oscillations.

For the next contours (12–50), a large discrepancy appears between numerical and experimental results. More specifically, the brick model and its submodel predicted an underestimated compressive force whereas the shell element predicted a tensile force. None of the FE models is refined enough to model the process accurately and predict the smallest force component. Even the very fine submodel, which uses the coarse global mesh as boundary conditions, cannot improve the radial stress state.

Figure 19 presents the predicted tangential component. An increase in the friction coefficient will increase the predicted force level. For this tangential component, the Lagamine shell simulations (`Sim1` to `4`) are less accurate than the global brick simulation (`Sim6`), which is in turn less accurate than the submodel simulations (`Sim8` and `10`). This seems logical since friction generates local shear strain and stress gradient through the thickness, which cannot be simulated by shell elements and are poorly described by the global brick model. The fact that, with a Coulomb friction coefficient of 0.05, all the models underestimate the absolute value of the transversal experimental force for the 20° cone while (as will be seen later in Fig. 22) they overestimate it for the 60° cone,

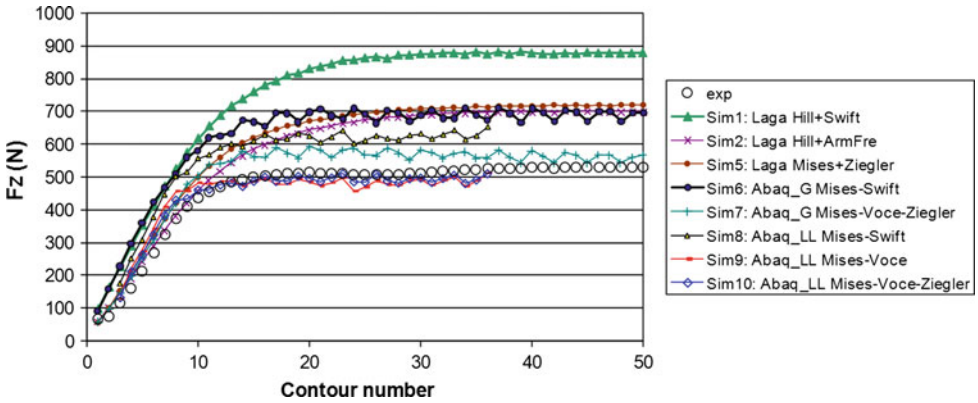

Fig. 20 Axial force for the 60° cone simulation

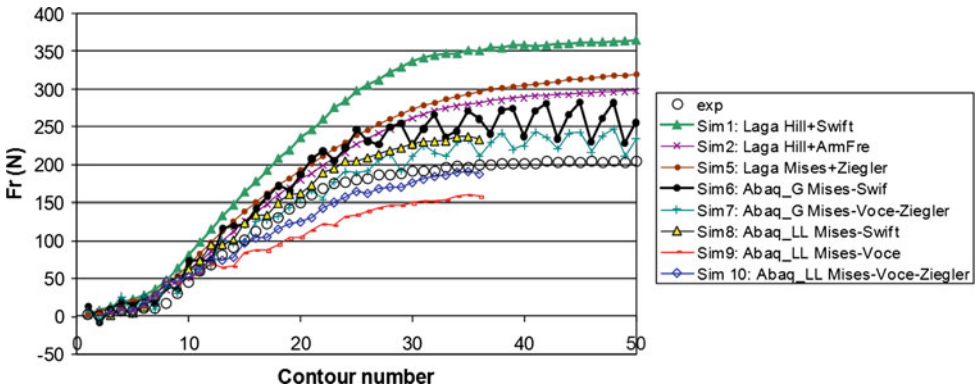

Fig. 21 Radial force for the 60° cone simulation

highlights the poor ability of these FE simulations to model the actual contact behavior.

As explained above, two contact zones with friction in different directions are separated by a point with no relative speed between the tool and the wall. These two zones do not compensate each other for the 20° cone, which explains the large (negative) experimental values. The FE simulations, which do not model the tool rotation and have an overly coarse a mesh (leading to poor contact conditions), cannot accurately reproduce the actual phenomenon [25].

5.3 FE force predictions for the 60° cone

The evolution of the experimental and predicted (8 simulations) axial tool force is shown in Fig. 20 for the 60° cone. Looking at the shell element simulations, it can be said that, as it was already the case for the 20° cone, the isotropic hardening generates an exceedingly high prediction (`Sim1`), which can be decreased by the use of kinematic hardening (`Sim2`).

The `Sim5` results confirm the fact that the choice of an isotropic or anisotropic yield locus and of the exact formulation of the kinematic hardening is negligible for this material.

While the `Sim2` results were close to experimental values for the 20° cone, it now presents an error of 40%. This result can be explained by the fact that for the 60° cone, the through-thickness shear is high (see Fig. 4 and Table 4), and it cannot be taken into account by the shell element.

For the five simulations performed with Abaqus and brick elements, the conclusions about the prediction of the total force can still be applied here for the axial force component shown in Fig. 20: the use of a submodel decreases the force prediction (as results from `Sim8` are lower than those from `Sim6`); for the global model, the use of kinematic and saturated isotropic laws also decrease the force prediction (as results from `Sim7` are lower than those from `Sim6`). The effect of the choice of hardening is stronger than that of the use of the submodeling technique (`Sim7` results lower `Sim8`). With the submodeling technique, saturated isotropic hardening (`Sim9`) strongly decreases the force prediction compared to Swift isotropic hardening (which is always increasing) as in `Sim8`.

Note that in the wall region of the 60° cone, accumulated equivalent engineering strains reached 200%, which explains why the choice of isotropic hardening (saturating or not) has such an influence on the result. It is surprising, however, that for the submodel with a saturating isotropic model, the use of a kinematic hardening law (`Sim10`) or not (`Sim9`) seems to have little effect: both results are quite similar and provide the best solution when compared with experimental values.

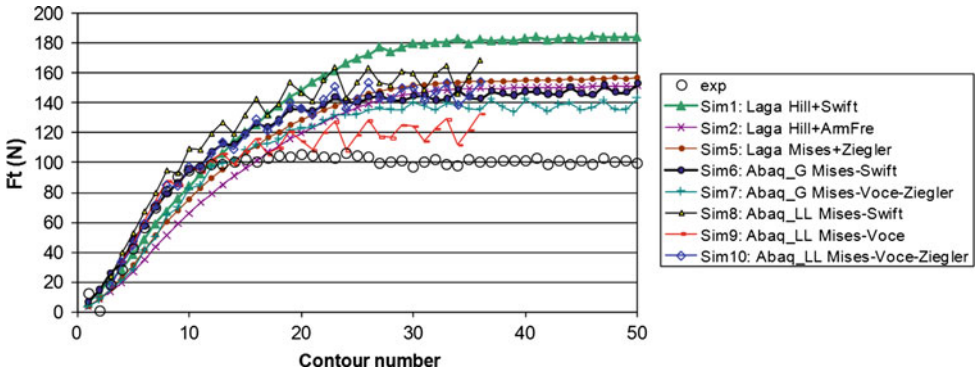

Fig. 22 Tangential force for the 60° cone simulation

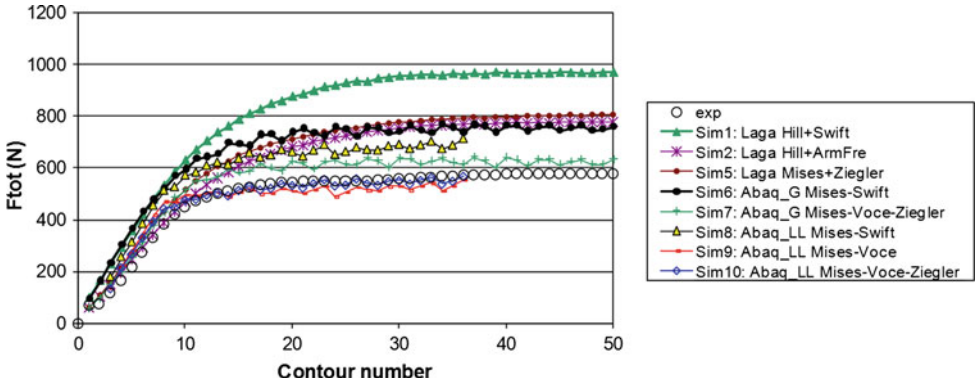

Fig. 23 Total force for the 60° cone simulation

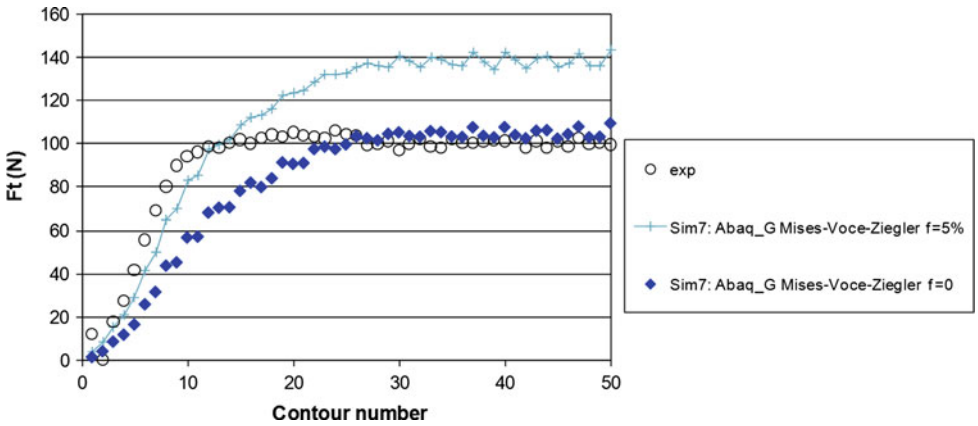

Fig. 24 Tangential force with and without friction for the 60° cone simulation

The evolution of the other force components (radial in Fig. 21 and tangential in Fig. 22) shows that kinematic hardening increases the predicted force level for the submodel (`Sim10` compared to `Sim9`) but decreases it for all the other simulations (`Sim2` or `Sim5` compared to `Sim1`; `Sim7` compared to `Sim6`).

For the submodel, the tangential force (Fig. 22) is less accurate with kinematic hardening (`Sim10`) than without (`Sim9`), while the opposite observation is made for the radial component (Fig. 21). As the relative weight of the radial component is higher than the tangential one for the 60° cone (see Table 5), Fig. 23's total force value shows a very slight advantage over `Sim10` (with kinematic hardening) compared with `Sim9` (without).

For Lagamine and Abaqus global simulations, the conclusions are different: the choice of kinematic hardening improves the prediction for each of the three force components (see Figs. 20, 21 and 22) and the best prediction is given with kinematic hardening.

Finally, Fig. 23 shows the effect of a change in the friction coefficient on the tangential force component. It can be observed that an accurate steady-state force component can

be reached by using a lower friction coefficient. The level reached by `Sim10` without friction is almost perfect. This result only proves that for the 60° cone, the two contact zones compensate each other but it does not mean that the true Coulomb friction coefficient is zero. As stated earlier, accurate modeling of the contact is not reached due to an overly coarse mesh and the absence of rotation of the tool.

6 Conclusion

The simulations and experiments performed show that the material flow is different for 20° and 60° cones, resulting in different stress and strain states.

In addition, the line test force prediction confirms that including an inverse approach with an indent test and fitting the material parameter with the finite element used are key factors in accurate force modeling in the SPIF process. All material data sets (Sets 5, 7 and 8) that provided numerical SPIF force predictions close to experimental values rely on such an identification procedure.

In the 20° cone, the model based on shell elements, which neglects through-thickness shear, could predict accurate axial forces provided that the material model take into account both isotropic and kinematic hardening and that an identification procedure uses an inverse approach including an indent test, which unlike classic tensile and shear tests, features sheet bending. The model based on brick elements with a fine mesh (submodel) did in fact provide results nearly as accurate as those using shell elements when using the same type of constitutive law.

For the 60° cone, only the brick FE models were able to model through-thickness shear, which takes place in the SPIF process. The amount of predicted shear depends on the mesh density, while the more finely meshed model (submodel) also shows more accurate force predictions.

For this large wall angle cone, it has been clearly demonstrated that a saturating hardening law such as Voce's is essential for accurate force prediction for the aluminum alloy used. A less significant improvement in force prediction can be seen when taking into account kinematic hardening.

In this study, the highest accuracy was reached in the case where brick elements with a fine mesh were used with a material model that combined the isotropic yield locus of von Mises with the mixed isotropic–kinematic hardening model of Voce–Ziegler.

Acknowledgments The authors gratefully acknowledge the financial support from the Institute for the Promotion of Innovation by Science and Technology in Flanders (IWT) and from the Interuniversity Attraction Poles Program from the Belgian State through the Belgian Science Policy agency, contract IAP6/24. In addition, as Research Director, A.M. Habraken would like to thank the Fund for Scientific Research (FNRS, Belgium) for its support.

References

1. Duflou JR, Lauwers B, Verbert J, Tunckol Y, de Baerdemaker H (2005) Achievable accuracy in single point incremental forming: case studies. In: Banabic D (ed) Proceedings of the 8th esaform conference, vol 2, pp 675–678, Bucharest
2. Hirt G, Junk S, Witulski N (2002) Incremental sheet forming: quality evaluation and process simulation. In: Proceedings of the 7th ICTP conference, vol 1, pp 925–930
3. Jeswiet J, Hagan E (2001) Rapid proto-typing of a headlight with sheet metal. In: Proceedings of the 9th international conference on sheet metal, pp 165–170, Leuven, April 2001
4. Leach D, Green AJ, Bramley AN (2001) A new incremental sheet forming process for small batch and prototypes parts. In: Proceedings of the 9th international conference on sheet metal, pp 211–218, Leuven, April 2001
5. Yoon SJ, Yang DY (2003) Development of a highly flexible incremental roll forming process for the manufacture of a doubly curved sheet metal. CIRP Ann Manuf Technol 52:201–204. doi:10.1016/S0007-8506(07)60565-4
6. Duflou JR, Sol H, Van Bael A, Habraken AM (2003) Description of the SeMPeR project (Sheet Metal oriented Prototyping and Rapid manufacturing), SBO-project financed by the IWT institute
7. He S, Van Bael A, Van Houtte P, Szekeres A, Duflou JR, Henrard C, Habraken AM (2005) Finite element modeling of incremental forming of aluminum sheets. Adv Mater Res 6–8:525–532
8. Aerens R, Eyckens P, Van Bael A, Duflou JR (2009) Force prediction for single point incremental forming deduced from experimental and FEM observations. Int J Adv Manuf Technol. doi:10.1007/s00170-009-2160-2
9. Ambrogio G, Duflou JR, Filice L, Aerens R (2007) Some considerations on force trends in incremental forming of different materials. In: Proceedings of the 10th esaform conference, vol 907 of AIP conference proceedings, pp 193–198. doi:10.1063/1.2729510
10. Jeswiet J, Duflou JR, Szekeres A (2005) Forces in single point and two point incremental forming. Adv Mater Res 6–8:449–456
11. Petek A, Kuzman K, Kopac J (2005) Forces and deformations analysis of incremental sheet metal forming. In: Proceedings of the 11th CAM^{3}S conference, Gliwice-Zakopane, Poland
12. Silva MB, Skjoedt M, Martins PAF, Bay N (2008) Revisiting the fundamentals of single point incremental forming by means of membrane analysis. Int J Mac Tools Manuf 48(1):73–83. doi:10.1016/j.ijmachtools.2007.07.004
13. Duflou JR, Tunçkol Y, Aerens R (2007) Force analysis for single point incremental forming. Key Eng Mater 344:543–550
14. Flores P, Duchêne L, Bouffioux C, Lelotte T, Henrard C, Pernin N, Van Bael A, He S, Duflou J, Habraken AM (2007) Model identification and FE simulations: effect of different yield loci and hardening laws in sheet forming. Int J Plast 23:420–449. doi:10.1016/j.ijplas.2006.05.006
15. Eyckens P, Del-lero Moreau J, Duflou JR, Van Bael A, Van Houtte P (2009) Marciniak-Kuczynski modelling of sheet formability in the incremental sheet forming process, taking into account through-thickness shear. In: Proceedings of the 12th ESAFORM2009 conference on material forming. Int J Mater Form Enschede, Netherlands. 2 (Suppl 1): 379–382
16. Emmens WC, van den Boogaard AH (2007) Strain in shear, and material behaviour in incremental forming. Key Eng Mater 344:519–526
17. Allwood JM, Shouler DR, Tekkaya AE (2007) The increased forming limits of incremental sheet forming processes. Key Eng Mater 344:621–628
18. Allwood JM, Shouler DR (2009) Generalised forming limit diagrams showing increased forming limits with non-planar stress

states. Int J Plast 25(7):1207–1230. doi:10.1016/j.ijplas.2008.11.001
19. Eyckens P, Van Bael A, Van Houtte P (2009) Marciniak-Kuczynski type modelling of the effect of through-thickness shear on the forming limits of sheet metal. Int J Plast 25(12):2249–2268. doi:10.1016/j.ijplas.2009.02.002
20. Eyckens P, Van Bael A, Van Houtte P (2008) An extended Marciniak–Kuczynski forming limit model to assess the influence of through-thickness shear on formability. In: Hora P (ed) Proceedings of the 7th numisheet conference, vol A, pp 193–198, Interlaken, Switzerland, September 2008
21. Emmens WC, van den Boogaard AH (2009) An overview of stabilizing deformation mechanisms in incremental sheet forming. J Mater Process Technol 209(8):3688–3695. doi:10.1016/j.jmatprotec.2008.10.003
22. Jeswiet J, Micari F, Hirt G, Bramley AN, Duflou JR, Allwood J (2005) Asymmetric single point incremental forming of sheet metal. CIRP Ann Manuf Technol 54(2):88–114. doi:10.1016/S0007-8506(07)60021-3
23. Website of Uddeholm (http://www.uddeholm.com) (2009) manufacturer of the Vanadis 23 tools. Last visited in November 2009
24. Duflou JR, Szekeres A, Vanherck P (2005) Force measurements for single point incremental forming: an experimental study. Adv Mater Res 6–8:441–448
25. Eyckens P, Belkassem B, Henrard C, Gu J, Sol H, Habraken AM, Duflou JR, Van Houtte P, Van Bael A (2010) Strain evolution in the single point incremental forming process: digital image correlation measurement and finite element prediction. Int J Mate Form. doi:10.1007/s12289-010-0995-6
26. Duflou JR, Verbert J, Belkassem B, Gu J, Sol H, Henrard C, Habraken AM (2008) Process window enhancement for single point incremental forming through multi-step toolpaths. CIRP Ann Manuf Technol 57:253–256. doi:10.1016/j.cirp.2008.03.030
27. Cescotto S, Grober H (1985) Calibration and application of an elastic viscoplastic constitutive equation for steels in hot-rolling conditions. Eng Comput 2(2):101–106. doi:10.1108/eb023607
28. Wang J, Wagoner RH (2004) A new hexahedral solid element for 3D FEM simulation of sheet metal forming. In: Ghosh S, Castro JC, Lee JK (eds) Proceedings of the 8th numiform conference, vol 712 of AIP conference proceedings, pp 2181–2186, Columbus, OH, USA, The Ohio State University. doi:10.1063/1.1766858
29. Duchêne L, El Houdaigui F, Habraken AM (2007) Length changes and texture prediction during free end torsion test of copper bars with FEM and remeshing techniques. Int J Plast 23:1417–1438. doi:10.1016/j.ijplas.2007.01.008
30. Habraken AM, Cescotto S (1998) Contact between deformable solids, the fully coupled approach. Math Comput Model 28(4–8):153–169. doi:10.1016/S0895-7177(98)00115-0
31. Li K (1995) Contribution to the finite element simulation of three-dimensional sheet metal forming. PhD thesis, University of Liège, Belgium. http://bictel.ulg.ac.be
32. Jaamei S, Frey F, Jetteur P (1989) Nonlinear thin shell finite element with six degrees of freedom per node. Comput Methods Appl Mech Eng 75(1–3):251–266. doi:10.1016/0045-7825(89)90028-5
33. Bouffioux C, Henrard C, Gu J, Duflou JR, Habraken AM, Sol H (2007) Development of an inverse method for identification of materials parameters in the single point incremental forming process. In: Tisza M (ed) Proceedings of the IDDRG 2007 conference, Győr, Hungary
34. Bouffioux C, Eyckens P, Henrard C, Aerens R, Van Bael A, Sol H, Duflou JR, Habraken AM (2008) Identification of material parameters to predict single point incremental forming forces. Int J Mater Form. doi:10.1007/s12289-008-0183-0
35. Bouffioux C, Henrard C, Eyckens P, Aerens R, Van Bael A, Sol H, Duflou JR, Habraken AM (2008) Comparison of the tests chosen for material parameters identification to predict single point incremental forming forces. In: Proceedings of the IDDRG 2008 conference, vol 1, pp 133–144, Olofström, Sweden
36. Henrard C (2005) Development of a contact model adapted to incremental forming. Master's thesis, University of Liège. Supervisor: Dr. Anne Marie Habraken
37. Eyckens P, He S, Van Bael A, Van Houtte P, Duflou J (2007) Forming limit predictions for the serrated strain paths in single point incremental sheet forming. In: Proceedings of the 9th numiform conference, vol 908 of AIP conference proceedings, pp 141–146. doi:10.1063/1.2740802
38. Eyckens P, Van Bael A, Aerens R, Duflou JR, Van Houtte P (2008) Small-scale finite element modelling of the plastic deformation zone in the incremental forming process. Int J Mater Form. doi:10.1007/s12289-008-0186-x
39. Lemaître J, Chaboche J-L (1985) Mécanique des matériaux solides. Dunod, Paris
40. Dennis JE, Schnabel RB (1983) Numerical methods for unconstrained Optimization and Nonlinear Equations. Prentice Hall, Englewood Cliffs
41. Rabahallah M, Bouvier S, Balan T, Bacroix B (2009) Numerical simulation of sheet metal forming using anisotropic strain-rate potentials. Mater Sci Eng A 517(1–2):261–275. doi:10.1016/j.msea.2009.03.078
42. Kocks UF, Mecking H (2003) Physics and phenomenology of strain hardening: the FCC case. Prog Mater Sci 48(3):171–273. doi:10.1016/S0079-6425(02)00003-8
43. Henrard C (2009) Numerical simulations of the single point incremental forming process. PhD thesis, University of Liège, Belgium. http://bictel.ulg.ac.be